Hierarchical micro-to-macroporous silica nanoparticles obtained by their grafting with hyper-crosslinked resin

Marco Guerritore[a,†], Federico Olivieri[a,†], Roberto Avolio[a], Rachele Castaldo[a,*], Mariacristina Cocca[a], Maria Emanuela Errico[a], Marino Lavorgna[b], Brigida Silvestri[c], Veronica Ambrogi[c], Gennaro Gentile[a]

[a] Institute for Polymers Composites and Biomaterials, National Research Council of Italy, Via Campi Flegrei 34, 80078 Pozzuoli, Italy

[b] Institute for Polymers Composites and Biomaterials National Research Council of Italy P.le E. Fermi 1, 80055 Portici, Italy

[c] Department of Chemical, Materials and Production Engineering, University of Naples, Piazzale Tecchio 80, 80125 Napoli, Italy

[†]These authors contributed equally to this work

*Corresponding author. E-mail address: rachele.castaldo@cnr.it

Abstract

In this work, mesoporous silica nanoparticles (MSN) hybridized with an organosilane are grafted with hyper-crosslinked poly(vinylbenzyl chloride) (PVBC), which is anchored into the mesopores and onto the external surface of MSN. The obtained nanoparticles are characterized by a MSN-templated hierarchical porosity composed of micropores, mesopores and macropores originated from the hyper-crosslinking of the PVBC phase, with a microporous fraction reaching up to 28 % of the total pore volume. Tested for the adsorption of a model dye (Rhodamine 6G, Rh6G), these nanoparticles result much more efficient in Rh6G adsorption with respect to plain MSN, showing a Rh6G uptake of about 125 mg/g in highly concentrated solutions (1000 mg/L) and quite complete removal (about 98 %) of the dye in more diluted conditions (30 mg/L) with

comparable efficiency in repeated adsorption cycles. Overall results demonstrate the key role of the hierarchical porosity of the hyper-crosslinked PVBC-grafted MSN to tailor their adsorption properties.

Keywords: mesoporous silica nanoparticles; hyper-crosslinked resin; hierarchical porosity; microporosity; dye adsorption.

1. Introduction

Hierarchically porous materials are broadly defined as those containing pores on multiple length scales, from macro- (>50 nm), to meso- (2–50 nm) and micro- (<2 nm) pore size [1]. This class of materials is very appealing for a wide range of applications, such as catalysis [2, 3], energy storage [4,5], drug delivery [6-8] and water and air remediation [9-11], due to the peculiar combination of improved transport phenomena in larger pores and remarkable adsorption properties of the smaller pores [12, 13]. Several examples of hierarchically porous systems are reported in literature, mainly based on two different designs: (i) composite systems which contain at least two phases characterized by different porosity [14] and (ii) hierarchical monomaterial or hybrid structures with a gradual interconnectivity amongst different pore levels [15].

Silica-based porous materials - in particular mesoporous silica nanoparticles (MSN) - represent an interesting solution for several of the above cited applications, thanks to their tuneable size [16], well-defined pore structures, high specific surface area (SSA) [17] and chemical stability [18]. In fact, MSN have been effectively used as nanocarriers of active agents, for instance drugs [19, 20] and corrosion inhibitors [21-23] or as adsorbent materials [24]. Nevertheless, to enhance the adsorption capacity of silica-based mesoporous materials, approaches aimed at creating hierarchical porosity in MSN have been proposed. For instance, methods based on silica precursors with properly selected functional groups combined with the application of structure directing agents have been developed for the realization of controlled macro-, meso- and microporosity [25] and enhanced adsorption of specific class of pollutants [26]. Moreover, silica nanoparticles characterized by ordered macropores with micro-/mesoporous honeycomb walls were obtained by an ice-templating technique combined to hydrothermal treatments [27].

With another approach, MSN were embedded in a divinylbenzene/vinylbenzyl chloride hyper-crosslinked resin obtaining hyper-crosslinked nanocomposites showing high SSA, increased microporosity and enhanced adsorption capacity towards organic pollutants dissolved in water [28]. Indeed, hyper-crosslinked resins are a class of polymers very attractive for their adsorption properties due to their micro-/mesoporous structure, realized through the creation of numerous methylene bridges between neighbouring aromatic rings during the hyper-crosslinking reaction. In contrast to the very ordered porous channels of mesoporous silica

nanoparticles, these resins are characterized by amorphous porosity in the micro- and mesoporous range. Also, they are very interesting for adsorption application for their narrow porosity and for the high tunability of the size and functionality of their porosity [11, 14, 29].

As a matter of fact, the development of new advanced adsorbent materials has recently become a very relevant research topic aimed towards the removal of hazardous organic contaminants derived from human productive activities from wastewater, thus developing new sustainable water treatment strategies and processes. In this context, in order to test the newly developed materials adsorption capacity towards organic contaminants, different types of model pollutants are usually selected in research experiments. In particular, synthetic dyes represent a category of pollutants that are very dangerous for the environment, because they have demonstrated to be very persistent to degradation and, even at low concentration, they significantly prevent the use, or reuse, of water. For example, xanthenic dyes stand out as candidate model dyes, since these dyes are largely used to synthesize drugs and to prepare dyes of the fluorescein and eosin class. Among these, rhodamine 6G (Rh6G) is a cationic polar dye with a rigid heterocyclic structure which exhibits a strong absorption in the visible and an intense fluorescence, and has been largely used as model organic pollutant for different adsorbent materials [14, 30-33].

In this work, we propose a new approach that, starting from properly functionalized MSN, leads to the creation of micropores into the nanoparticles mesopores and new meso- and macropores on the external surface of the MSN, by grafting and hyper-crosslinking a vinylbenzyl chloride precursor resin. In this way, MSN are used as a template for the realization of hierarchical micro/meso/macroporous silica/polymer structures. In particular, MSN functionalized with different amount of vinyl moieties are realized through a one-step high yield and high throughput synthetic procedure. The vinyl functionalities of nanoparticles are exploited to graft poly(vinylbenzyl chloride) by in-situ polymerization and the resulting polymer phase is subjected to hyper-crosslinking through Friedel-Crafts reaction. The morphology, structure and textural properties of the synthesized nanoparticles is investigated through a multitechnique approach. Finally, the hierarchically porous nanoparticles are tested, in comparison to plain MSN, for the adsorption of organic aromatic contaminants from water, using Rh6G as a model pollutant.

2. Experimental section

2.1 Materials

Vinylbenzyl chloride (VBC, ≥95.0%, mixture of isomers, ~70% meta + ~30% para), 2,2'-azobis(2-methylpropionitrile) (AIBN, >98%), tetraethyl orthosilicate (TEOS, 99.999%), cetyltrimethylammonium bromide (CTAB, ≥99%), triethanolamine (TEA, ≥ 99%), vinyl-trimethoxysilane (VTMOS, >98%), rhodamine 6G (Rh6G), hydrochloric acid (HCl, 37 wt%), $FeCl_3$ (≥97%), 1,2-dichloroethane (DCE) and all solvents were purchased from Sigma-Aldrich (Milan, Italy) and used without further purification. Bi-distilled water was used for all the laboratory procedures.

2.2 Synthesis of vinyl-functionalized mesoporous silica nanoparticles

Organic functionalized mesoporous silica nanoparticles were realized by a one-step reaction. In the specific, 1 g of CTAB and 57 g of TEA were dissolved in 70 g of distilled water and mixed for 1 hour at 80 °C and 1200 rpm. Then, a total amount of 10 g of TEOS and VTMOS were added in the 95:5, 90:10 and 80:20 TEOS:VTMOS weight ratio. In particular, TEOS was added first in order to induce its pre-hydrolysis and VTMOS was added after 10 minutes. The solution was kept under stirring for 1.5 hour, the product obtained was then filtered on filter paper and washed with 0.5 L of 1.5 M ethanol/HCl solution. Finally, the product was washed with distilled water until neutrality, collected through filtration and placed in an oven at 80 °C under vacuum overnight. The resulting products were coded MSN_xVTMOS, where x represents the weight percent of VTMOS employed.

Furthermore, plain mesoporous silica nanoparticles (MSN) were synthesized following the procedure indicated above but without adding VTMOS, therefore using 10 g of TEOS, in order to get a non-functionalized sample to be used as a reference to evaluate the effect of the functionalization on the textural and adsorption properties of the nanoparticles.

Yield of reaction for MSN and MSN_xVTMOS was evaluated on the basis of the TEOS/VTMOS reaction mixture composition and the stoichiometry of the reaction. The contribute of terminal hydroxyl groups was omitted by approximating the chemical formula of plain MSN to SiO_2 and the chemical formula of the product of VTMOS after hydrolysis and condensation to $SiO_{1.5}CH{=}CH_2$.

2.3 Grafting of hyper-crosslinked resin onto mesoporous silica nanoparticles

Poly(vinylbenzyl chloride) (PVBC) was grafted on MSN_xVTMOS by free radical polymerization. MSN_xVTMOS were dispersed in vinylbenzyl chloride by ultrasonication with a tip Sonics Vibracell ultrasonic processor (500 W, 20kHz; Newton, USA) at 25% power with an ON/OFF cycle of 10s/50s for 10 minutes, while the dispersion was kept in an ice/water bath. Then, free radical polymerization of VBC was started by adding 0.5 phr of AIBN and the mixture was stirred at 80 °C, under nitrogen flow. This stage was prolonged until the mixture viscosity increased enough to hinder nanoparticles re-aggregation (about 1.5 hour), and then the polymerization was completed in oven for 24 h at 80 °C. The obtained nanoparticles were washed twice with dichloroethane in order to dissolve the excess of unbound polymer and recovered by centrifugation at 13000 rpm and 4 °C for 10 minutes. Then, the obtained samples were placed in oven at 80 °C under vacuum overnight. The resulting products were coded MSN_xPVBC, correspondingly to the precursors MSN_xVTMOS.

The grafted PVBC phase of MSN_xPVBC was subjected to hyper-crosslinking via Friedel-Crafts reaction. MSN_xPVBC (0.4 g) were stirred in DCE (40 g) for 2 h, under nitrogen. Then, the mixture was cooled to 0 °C in an ice/water bath, $FeCl_3$ (2 g) was added and the reaction mixture was kept stirring for 2 h. Finally, the system was heated to 80 °C for 18 h. The obtained materials were repeatedly washed with methanol and dried under vacuum at 80 °C overnight. The samples thus obtained were coded X_MSN_xPVBC, where the prefix X_ denotes the hyper-crosslinking.

2.4 Characterization

MSN_xVTMOS, pVBC, MSN_xPVBC and X_MSN_xPVBC were analyzed by FTIR in attenuated total reflection (ATR) mode. Spectra were recorded with a PerkinElmer Spectrum One FTIR spectrometer equipped with an ATR module, using a resolution of 4 cm^{-1} and 32 scan collections.

MSN_xVTMOS, MSN_xPVBC and X_MSN_xPVBC were analyzed by solid-state ^{13}C CP-MAS NMR, using a Bruker Avance II 400 spectrometer equipped with a 4 mm magic angle spinning (MAS) probe. Samples were

136 packed in 4 mm zirconia rotors sealed with Kel-F caps and rotated at a spinning speed between 8 and 9 kHz.
137 A ^{1}H π/2 pulse width of 3.6 μs, a contact time of 2 ms and a repetition time of 5 s were used.
138 Bright field transmission electron microscopy (TEM) analysis was performed on MSN_xVTMOS, MSN_xPVBC
139 and X_MSN_10PVBC using a FEI Tecnai G12 Spirit Twin (LaB6 source) at 120 kV acceleration voltage. Images
140 were collected on a FEI Eagle 4k CCD camera. Before the analysis, the samples were dispersed in DCE by
141 ultrasonication with the above mentioned equipment for 2 min at 25% power. The samples were then
142 collected by immersing holey carbon-coated copper grids in the dispersions. Average diameters of the
143 nanoparticles were calculated through analysis of the collected image with the software ImageJ.
144 Thermogravimetric analysis was carried out on MSN_xVTMOS, pVBC, MSN_xPVBC and X_MSN_xPVBC using
145 a Perkin Elmer Pyris 1 thermogravimetric analyzer. All samples were analyzed in oxidizing atmosphere, at 10
146 °C/min heating rate, from 100 °C to 800 °C. A further scan in nitrogen atmosphere at 1 °C/min heating rate
147 from 100 °C to 800 °C was also collected on MSN_10VTMOS.
148 Gas adsorption volumetric analysis was performed on MSN, MSN_xVTMOS, MSN_xPVBC and X_MSN_xPVBC
149 using a Micromeritics ASAP 2020 analyzer. SSA was determined by nitrogen adsorption measurements at 77
150 K from the linear part of the Brunauer–Emmett–Teller (BET) equation. Prior to the analysis, all samples were
151 degassed at 100 °C under vacuum ($p < 10^{-5}$ mbar). All the adsorption measurements were performed using
152 high purity gases (> 99.999%). Nonlocal Density Functional Theory (NLDFT) was applied to nitrogen
153 adsorption isotherms to evaluate the pore size distribution of the nanoparticles. In particular, a cylindrical
154 pore model was applied for MSN, MSN_xVTMOS and MSN_xPVBC and a slit pore model was applied for the
155 hyper-crosslinked X_MSN_xPVBC.
156 Finally, MSN and X_MSN_10PVBC were tested for the adsorption of a reactive cationic dye from water,
157 rhodamine 6G. Tests were performed at 25 °C at different concentrations ranging from 30 mg/L to 1000
158 mg/L. Samples of 10 mg were added to 10 mL of dye solution, which was kept at 25 °C until equilibrium was
159 reached (at least 24 h). Then, the dye concentration in the supernatant was measured by a Jasco V570 UV-
160 Vis spectrophotometer, using a rhodamine 6G previously recorded calibration curve.
161 The amount of adsorbed dye (Q_e, mg/g) was determined using the equation:
162

$$Q_e = \frac{(C_0 - C_f)V}{m} \quad \text{(eq.1)}$$

where C_0 and C_f are the initial and final concentration of the dye solution, V is the volume of dye solution and m is the mass of the adsorbent.

Also, three cyclic adsorption/desorption tests were performed on X_MSN_10PVBC with a Rh6G solution at the initial concentration of 30 mg/L. Between adsorption cycles, the desorption of Rh6G was induced with ethanol washings performed in this way: after an adsorption test, the nanoparticles were left to settle on the bottom of the vial and the supernatant aqueous Rh6G solution was removed with a pipette; then, ethanol was added to the nanoparticles and the vial was placed on a shaker, inducing the desorption of Rh6G in the solvent; subsequently, the nanoparticles were left to settle again and the ethanol supernatant solution was replaced with fresh ethanol. Further washings with ethanol (about three in each case) were performed similarly, until the supernatant solution appeared completely transparent and the absence of appreciable amounts of Rh6G in the supernatant was verified by UV-Vis. Therefore, the nanoparticles were dried under vacuum and then were subjected to a subsequent adsorption cycle with the previously described modalities.

3. Results

3.1 Synthesis of vinyl-functionalized mesoporous silica nanoparticles

Vinyl-functionalized mesoporous silica nanoparticles are obtained through a one-step high yield sol-gel synthesis. Three different TEOS:VTMOS weigh ratio have been used for the synthesis, namely 95:5, 90:10 and 80:20, in order to optimize the relative amount of vinyl moieties in view of the grafting of the microporous resin. For all samples the reaction yield is quite high, ranging from 98 % for MSN to 96% for MSN_5VTMOS and to about 91% for MSN_10VTMOS and MSN_20VTMOS.

FTIR spectroscopy, shown in Figure 1a, reveals the characteristic absorption signals of silica for all the nanoparticles. In particular, MSN_xVTMOS spectra are characterized by the strong absorption band at 1050 cm^{-1} corresponding to the stretching vibration Si-O-Si, the peak at 970 cm^{-1} corresponding to the Si-OH bending vibration, and the peak at 780 cm^{-1} attributed to the symmetric Si-O-Si stretching [34]. Then,

absorption signals associated to vinyl moieties increase with increasing the VTMOS content, specifically the absorption bands centred at 1600 cm^{-1} and 1410 cm^{-1}, attributed to C=C vibration, and the absorption signals at 1010 cm^{-1} and 967 cm^{-1}, associated to the Si-O vibration of silicon atoms linked to vinyl carbon atoms [35].

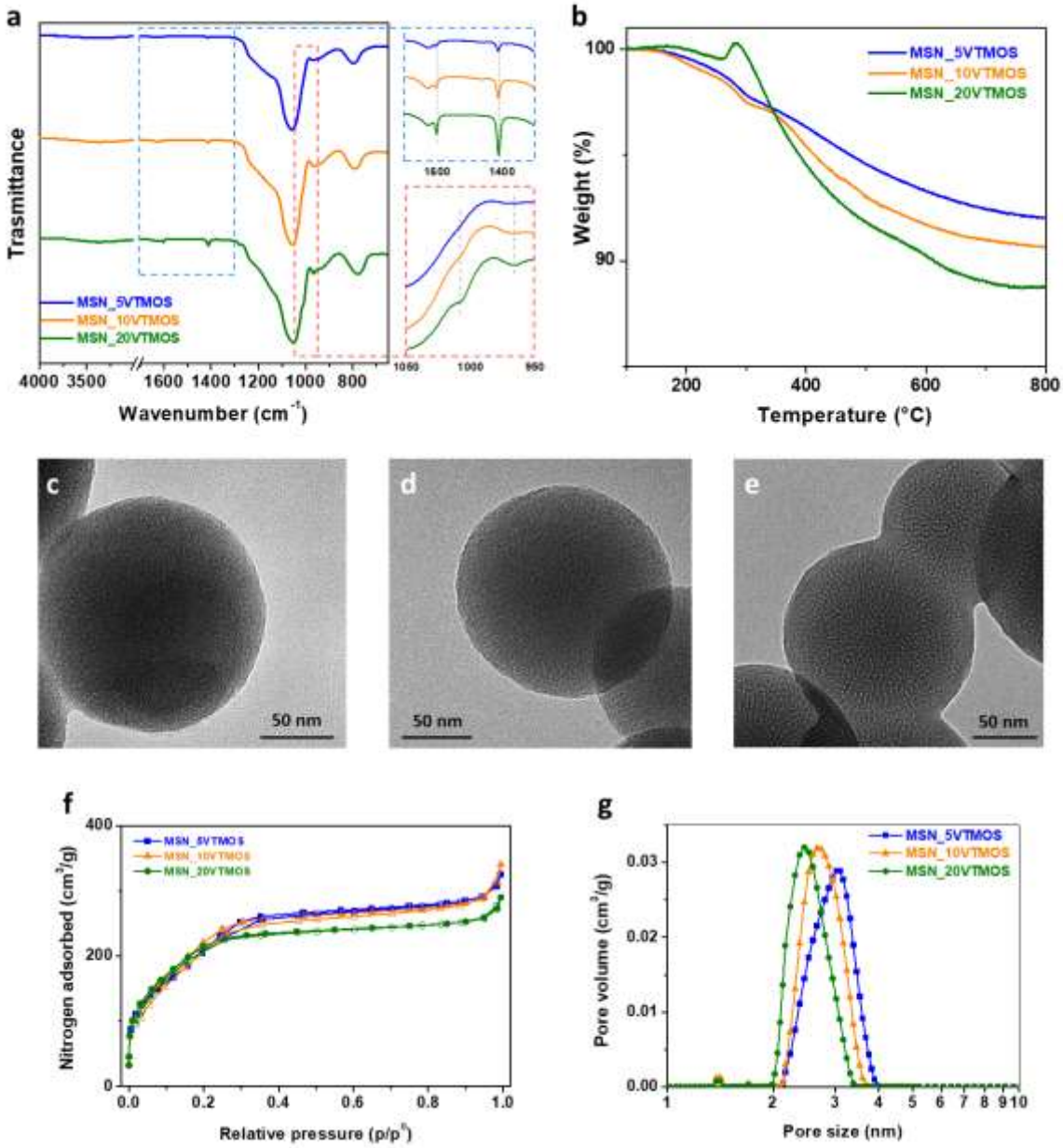

Figure 1. FT-IR spectrum (a) and TGA traces (b) of MSN_xVTMOS; TEM images of MSN_5VTMOS (c), MSN_10VTMOS (d) and MSN_20VTMOS (e); nitrogen adsorption (full symbols) and desorption (empty symbols) isotherms (f) and DTF pore size distribution (g) of MSN_xVTMOS.

198 Thermogravimetric analysis of MSN_xVTMOS performed in oxidative conditions confirms that the
199 nanoparticles are characterized by increasing amounts of organic moieties at increasing content of VTMOS
200 precursor, as shown by the increasing thermo-oxidative degradation of the nanoparticles (Figure 1b). Indeed,
201 the residual weights at 800 °C are 92.0 wt% for MSN_5VTMOS, 90.7 wt% for MSN_10VTMOS, and 88.8 wt%
202 for MSN_20VTMOS. To be noticed is that at the same temperature the residual weight is about 96.5 wt% for
203 plain MSN. A peculiar behaviour of the TGA curve is evidenced for the sample MSN_20VTMOS which, during
204 heating, shows a weight gain at temperature close to 300 °C, due to the oxidation of the vinyl groups [36].
205 In all cases, the TGA curves show a multistep degradation of the organic moieties of the MSN_xVTMOS
206 nanoparticles, clearly evidenced through the analysis of the TG and differential TG curve collected at low
207 heating rate (1°C/min, Figure S1) on the sample MSN_10VTMOS. Indeed, these curves well show that the
208 degradation occurs in multiple convoluted steps in the temperature ranges 110-800 °C with the last main
209 DTG peak centred at about 550 °C. Thus, the degradation of the organic moieties occurs in a temperature
210 range much wider than the ones reported for organosilanes grafted on non-porous silica nanoparticles [37,
211 38]. This phenomenon is ascribable to the presence of vinyl moieties both on the peripheral surface and on
212 the surface of the inner pores. Indeed, for MSN_xVTMOS, the nanoparticles porous structure acts as a
213 physical barrier able to hinder the degradation of the organic functionalities present in the inner pores [39].
214 As observed by TEM analysis (Figure 1c-e), all MSN_xVTMOS show a spherical morphology with geminal
215 structure and very ordered worm-like porous channels. MSN_5VTMOS, MSN_10VTMOS and MSN_20VTMOS
216 show an average diameter of 173 ± 19 nm, 151 ± 23 nm, and 160 ± 22 nm, respectively. The VTMOS content
217 does not significantly alter the structure of the nanoparticles. Only a thin (1-2 nm) layer characterized by
218 higher contrast is observed on the nanoparticles outer surface, whose thickness slightly increases with the
219 increase of the VTMOS content. The presence of the external layer is more evident for the sample
220 MSN_20VTMOS, this finding being in agreement with the TGA results, revealing the presence of a more
221 consistent organic phase for this sample.
222 N_2 adsorption analysis of MSN_xVTMOS shows that all nanoparticles are characterized by a type IV isotherm
223 (Figure 1f), typical of mesoporous materials with very ordered porosity and comparable to the MSN isotherm
224 (Figure S2a). The total pore volume of the functionalized nanoparticles and the nanoparticles pores diameter

decrease with the extent of functionalization (Figure 1g). While plain MSN pores diameter distribution is centred around 3.48 nm (Figure S2b), in MSN_5VTMOS, MSN_10VTMOS and MSN_20VTMOS the pores diameter distributions are centred at 3.1 nm, 2.7 nm and 2.5 nm, respectively. No significant differences on the BET SSA of the nanoparticles is shown for VTMOS content up to 10 %, explainable with the fact that together with the volume reduction, MSN_5VTMOS and MSN_10VTMOS are also characterized by smaller pores with respect to MSN, giving rise to slightly higher SSA. At higher VTMOS content, instead, a further but very limited reduction of the nanoparticles pore size is associated to a moderate reduction of pore volume and SSA.

Table 1. BET SSA and porosity of MSN, MSN_xVTMOS and X_MSN_xPVBC

Sample	BET SSA (m^2/g)	Total pore volume (cm^3/g)	Micropore fraction (%)
MSN	810 ± 15	0.49	-
MSN_5VTMOS	824 ± 19	0.42	-
MSN_10VTMOS	825 ± 20	0.40	-
MSN_20VTMOS	785 ± 17	0.37	-
X_MSN_5PVBC	297 ± 5	0.25	27.9
X_MSN_10PVBC	420 ± 7	0.45	22.9
X_MSN_20PVBC	245 ± 4	0.26	22.3

3.2 Grafting of precursor resin onto mesoporous silica nanoparticles

The vinyl functionalities of MSN_xVTMOS were exploited to graft the PVBC phase on the MSN surface by in-situ polymerization of vinylbenzyl chloride. A schematic representation of this reaction is reported In Figure 2 (I step).

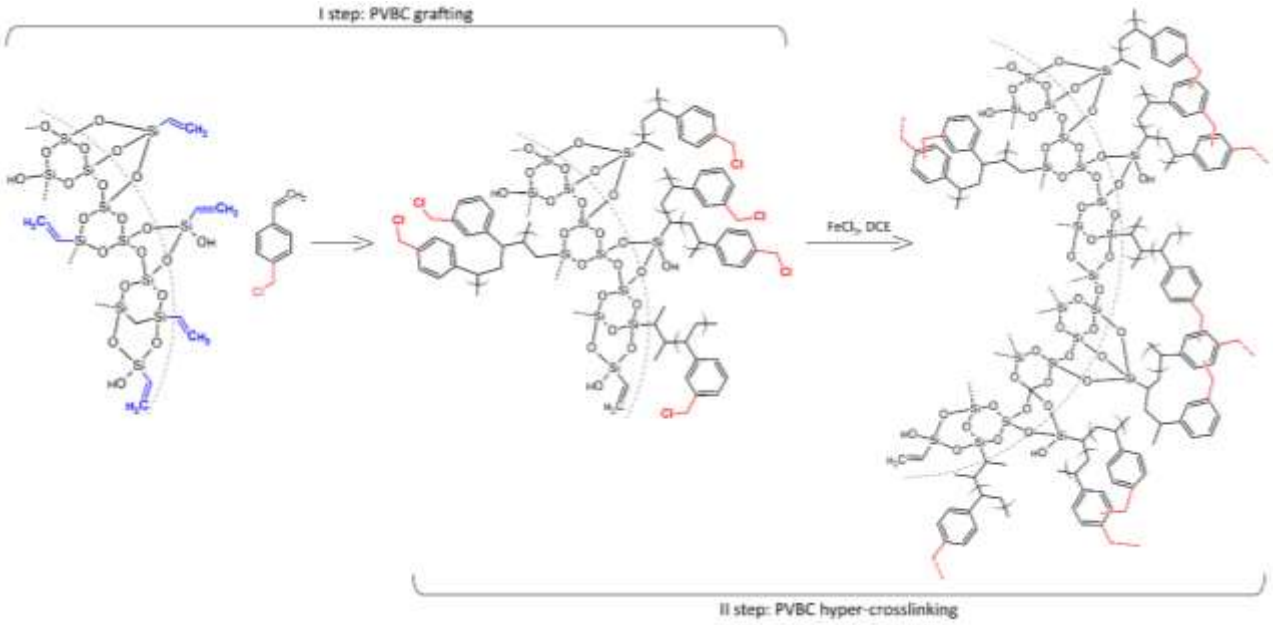

242

243 **Figure 2**. Scheme of reaction of PVBC grafting onto MSN_xVTMOS (I step) and following hyper-crosslinking

244 (II step).

245

246 The effectiveness of the PVBC grafting is confirmed by FTIR and NMR analysis of the functionalized

247 nanoparticles. Indeed, the analysis of MSN_xPVBC by FTIR spectroscopy shows the typical PVBC signals in the

248 range 3200-1300 cm^{-1}, attributed to C-H and C=C vibrations, a signal at 1265 cm^{-1} due to the $-CH_2$-Cl

249 stretching, evidenced as a shoulder of the main Si-O-Si peak, and the C-Cl vibration signals at 708 and 675

250 cm^{-1} (Figure 3a) [40]. Likewise, ^{13}C CP/MAS NMR spectra of MSN_xPVBC show the typical PVBC signals, with

251 a fairly well resolved aromatic region and the evident chloromethyl signal centred at 47 ppm, superimposed

252 to the broad peak of the saturated backbone (Figure 3b) [29]**Errore. Il segnalibro non è definito.**.

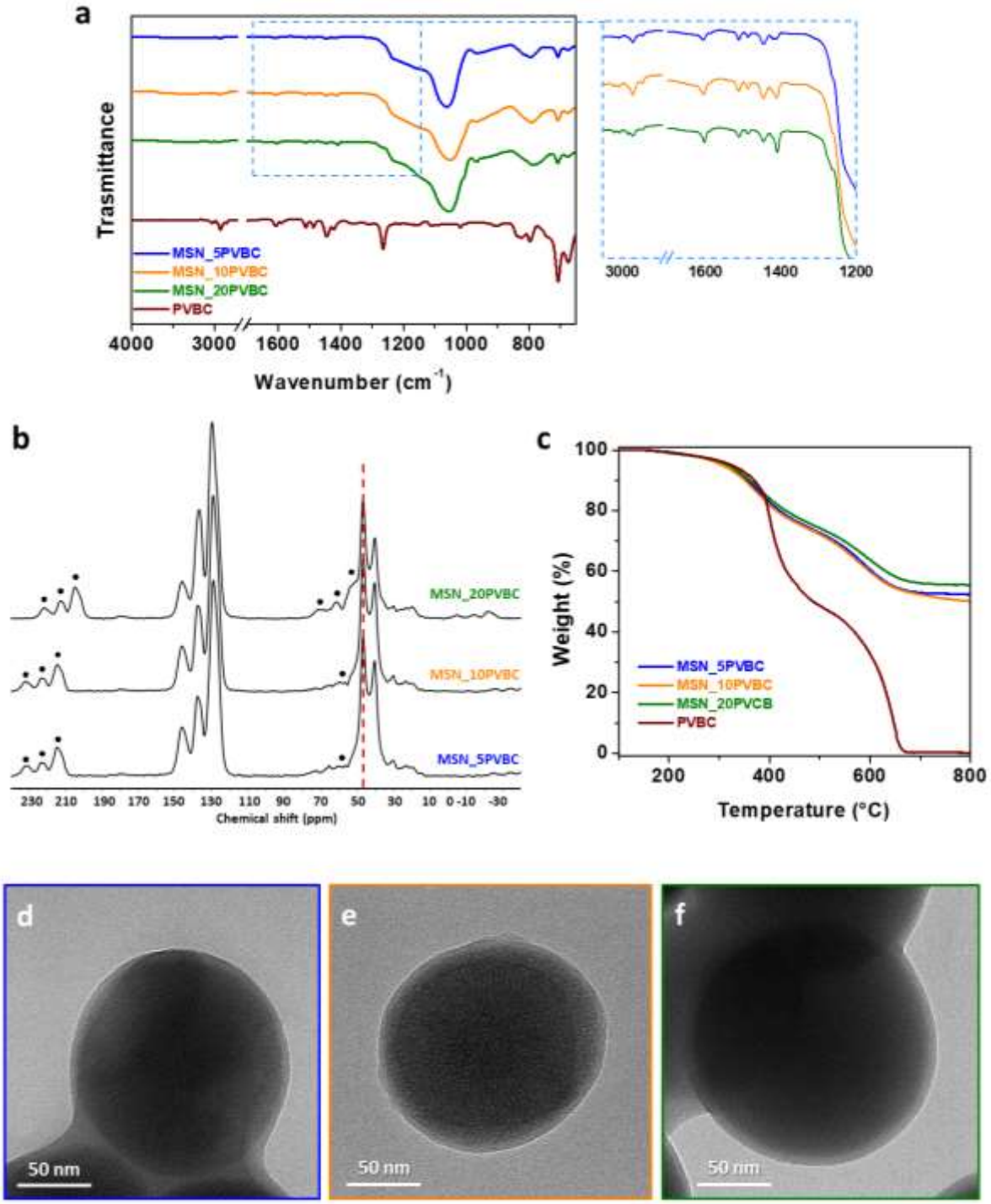

253

254 **Figure 3**. FTIR (a) and NMR spectra (b, the position of the CH_2Cl resonance is indicated by a dashed line,

255 spinning sidebands are marked by dots) of MSN_xPVBC; TGA traces of MSN_xPVBC (c); TEM images of

256 MSN_5PVBC (d), MSN_10 PVBC (e) and MSN_20 PVBC (f)

257

Thermogravimetric analysis of MSN_xPVBC (Figure 3c) shows for all samples two degradation steps at 400 °C and 620 °C, ascribable to the grafted PVBC phase. All samples show a quite comparable weight loss, in the range of 45-50 wt%, which is to be attributed to the polymer phase. In particular, although the MSN_xVTMOS nanoparticles are characterized by varying amounts of vinyl moieties, TGA indicates that the amount of PVBC grafted on MSN_5PVBC and MSN_10PVBC is similar (weight loss at 800 °C about 50 wt%), while at the same temperature MSN_20PVBC shows about 45 wt% weight loss, indicating a slightly lower grafting efficiency.

For all MSN_xPVBC samples, the grafted PVBC phase is noticeable in TEM images as a diffuse shell of thickness between 5 nm and 10 nm, which covers the silica nanoparticles. Also, the typical ordered porosity of mesoporous silica nanoparticles appears less visible in TEM images of MSN_xPVBC, compared to the MSN_xVTMOS images, indicating that the PVBC phase is grafted also within the nanoparticles mesopores. Indeed, the PVBC grafting also induces a drastic decrease in the accessible porosity and SSA of the nanoparticles. N_2 adsorption measurements conducted on MSN_xPVBC show that the SSA of the nanoparticles is reduced to values lower than 10 m^2/g and their pore volume is not detectable (less than 0.01 cm^3/g). This result also indicates that the PVBC grafting reaction takes place on all the accessible surface of the nanoparticles where the vinyl functionalities are present, including both the external nanoparticle surface and the surface of the inner mesopores. Indeed, both internal and external surfaces of mesoporous silica are available to chemical functionalization, and specific protection mechanisms of the inner walls of the mesopores are needed when the selective functionalization of the external surface is desired [41].

3.3 Hyper-crosslinking of the grafted PVBC phase onto mesoporous silica nanoparticles

MSN_xPVBC were subjected to hyper-crosslinking through Friedel-Crafts reaction, obtaining the corresponding X_MSN_5PVBC, X_MSN_10PVBC, and X_MSN_20PVBC samples. In this phase, methylene bridges are installed between the aromatic rings of adjacent PVBC chains grafted onto the mesoporous silica nanoparticles. In this way, the grafted PVBC chains are locked into an interconnected configuration, creating new porosities into the pores and onto the surface of the MSN. A schematic representation of this reaction is reported in Figure 2 (II step). The occurrence of the hyper-crosslinking reaction in the PVBC phase is revealed by spectroscopic analyses. For all the hyper-crosslinked samples, FTIR spectra (Figure 4a) show a

285 significant attenuation of the peaks associated to the C-Cl vibration modes (708 and 675 cm^{-1}) in comparison
286 to the corresponding MSN_xPVBC, revealing that the hyper-crosslinking of the samples is effective. In
287 particular, while the signal at 675 cm^{-1} is almost completely undetected for all samples, the signal at 708 cm^{-1}
288 is much less intense in sample X_MSN_10PVBC, in comparison to X_MSN_5PVBC and X_MSN_20PVBC,
289 suggesting that at the intermediate TEOS:VTMOS composition the extent of hyper-crosslinking is the highest
290 achieved among the three samples. These results are confirmed by ^{13}C CP/MAS NMR (Figure 4b). Indeed,
291 while in all samples the main aromatic signals (110-160 ppm) result broadened upon hyper-crosslinking,
292 indicating a higher degree of substitution of the aromatic carbons, this effect is much more evident at the
293 intermediate composition X_MSN_10PVBC. Likewise, the chloromethyl signal (47 ppm) intensity decreases
294 in all samples with respect to the corresponding MSN_xPVBC spectra but only in the X_MSN_10PVBC sample
295 it is no more detectable, indicating a high yield of the hyper-crosslinking reaction [15, 29].

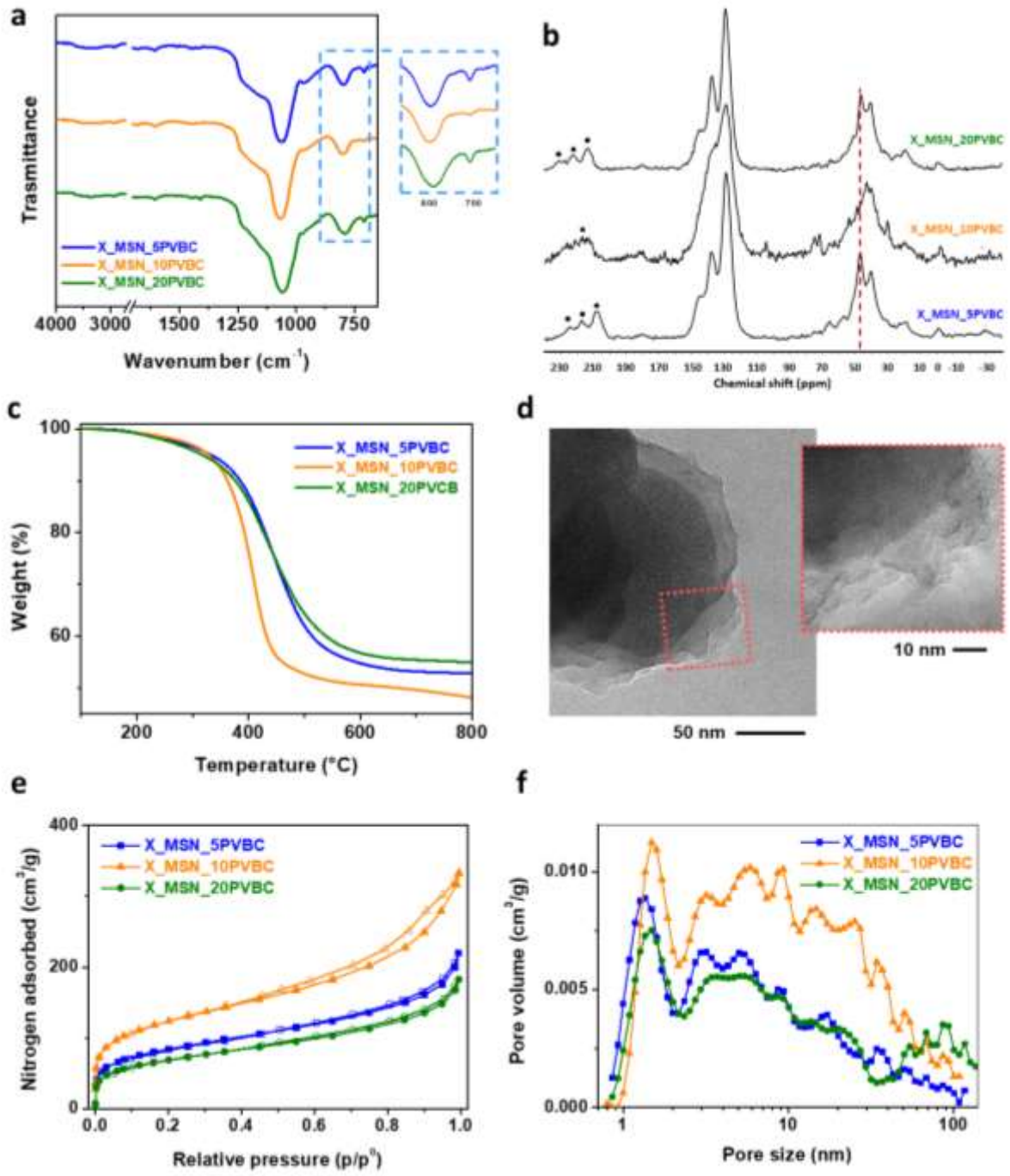

Figure 4. FTIR spectra (a), NMR spectra (b)and TGA traces (c) of X_MSN_xPVBC; in (b) , the position of the CH_2Cl resonance is indicated by a dashed line, spinning sidebands are marked by dots; TEM image of X_MSN_10PVBC (d); nitrogen adsorption (full symbols) and desorption (empty symbols) isotherms (e) and DTF pore size distribution (f) of X_MSN_xPVBC

TGA analysis of X_MSN_xPVBC is consistent with TGA results of MSN_xPVBC, showing a weight loss at 800 °C for all samples between 45 wt% and 50 wt% (Figure 4c), with lower weight loss, attributed to the grafted

304 organic phases, for X_MSN_20PVBC and progressively higher weight loss values for X_MSN_5PVBC and
305 X_MSN_10PVBC, respectively.
306 The hyper-crosslinked nanoparticles X_MSN_10PVBC morphology was observed by TEM analysis. TEM
307 images, shown in Figure 4d, show that the hybrid nanoparticles are surrounded by a consistent and diffuse
308 layer characterized by higher thickness (up to 30 nm) and less contrast with respect to the polymeric layer
309 revealed in MSN_xPVBC TEM images. This is to be ascribed to the swelling and the hyper-crosslinking of the
310 PVBC phase. Indeed, during these processes, the PVBC grafted chains of the nanoparticles increase their
311 volume, due to the uptake of dichloroethane. Then, through Friedel-Crafts reaction, the swollen polymer
312 phase is consolidated in this configuration through the installing of methylene bridges between neighbouring
313 aromatic rings. Through this process, micropores and mesopores typical of the hyper-crosslinked polymers
314 are formed [42, 43].
315 The analysis of the textural properties of the hyper-crosslinked nanoparticles confirms this mechanism, as
316 the presence of new micro-, meso- and macroporosity is revealed. Indeed, the X_MSN_xPVBC isotherms
317 (Figure 4e) have very different shape with respect to the curves of their MSN_xVTMOS precursors, showing
318 type II isotherms, typical of micro/mesoporous materials with a broad distribution of porosity. In fact,
319 X_MSN_xPVBC are characterized by a large distribution of porosity, ranging from 0.8 nm to 100 nm (Figure
320 4f). In particular, a major peak of microporosity is centred at about 1.5 nm, and a broad distribution of
321 porosity extends from 2 nm to 100 nm, constituting a hierarchically porous structure of interconnected
322 micropores, mesopores and macropores. This result further demonstrates that the grafting and hyper-
323 crosslinking of the PVBC phase takes place both in the mesopores of the hybrid silica nanoparticles and on
324 their peripheral surface. Indeed, in pore size distribution curves of X_MSN_xPVBC (Figure 4f) it is no more
325 evident the mesopores peak of pristine MSN_xVTMOS (Figure 1g) but, instead, a broad porosity ranging from
326 0.8 nm to 100 nm is measured by N_2 adsorption analysis. Since, as shown by FTIR and NMR analysis, the PVBC
327 phase is extensively crosslinked, it follows that the PVBC hyper-crosslinked phase has been grafted both into
328 the mesopores and onto the external surface of the nanoparticles. Therefore, by grafting and hyper-
329 crosslinking of PVBC into the MSN_xVTMOS mesopores, new microporosity is created. Then, while only pores
330 of dimension lower than the pristine MSN_xVTMOS pores (from 2.5 to 3.1 nm) can be created in the

polymeric phase grafted within the nanoparticles mesopores, wider pores are created on the outer surface of the nanoparticles, realizing in this way a MSN-templated hierarchical porous structure. This kind of porosity is very valuable for adsorption phenomena due to the reduction of diffusion hindrances [44]. Also, although X_MSN_xPVBC nanoparticles show lower BET SSA than the pristine silica nanoparticles MSN_xVTMOS, the presence in these sample of the newly generated micropores, especially within a hierarchically porosity, is very appealing for adsorption applications [14, 25] .

Among all hyper-crosslinked samples, X_MSN_10PVBC is characterized by the highest amount of porosity, with a total pore volume of 0.45 cm^3/g, showing also the highest BET SSA of 420 m^2/g (Table 1). As concerning the recorded differences amongst the three X_MSN_xPVBC samples in terms of hyper-crosslinking yield, as shown by spectroscopic analysis, and in terms of textural properties, the possible effect of the molecular weight of the grafted PVBC phase should be considered. Indeed, by varying the TEOS:VTMOS ratio in the MSN_xVTMOS series, the relative amount of vinyl moieties in the functionalized nanoparticles increases with the increase of VTMOS added to the reaction mixture. Nevertheless, by grafting the PVBC precursor through the in-situ polymerization of vinylbenzyl chloride, the increased amount of vinyl groups does not correspond to a significantly different amount of grafted PVBC. In fact, the MSN_5PVBC and the MSN_10PVCB samples show similar amounts of grafted organic phase (approximately 50 wt% by TGA) while a higher density of vinyl groups (MSN_20VTMOS) induces a slightly lower amount of grafted PVBC in the MSN_20PVBC sample. Therefore, taken into account the increased density of vinyl groups and the comparable amount of grafted PVBC, a reliable hypothesis is that, by progressively increasing the amount of vinyl groups installed on the precursor nanoparticles, PVBC chains with lower length are grafted [37]. Considering the well-established role of the chain lengths of polymer brushed tethered onto inorganic nanoparticles on their steric confinement, conformation and dynamical properties [45], this hypothesis well matches the results obtained after the hyper-crosslinking reaction. Indeed, in the chlorinated media used for hyper-crosslinking, longer PVBC chains grafted onto silica in MSN_5PVBC sample would result well extended from the nanoparticle surface, with an almost fully stretched conformation due to the enthalpic attraction between chains segments and solvent molecules and the entropic repulsion between chain segments [46]. On the contrary, by reducing the chain length of the grafted polymer brushes (MSN_20PVBC), the polymer chains would tend

towards a collapsed conformation, with the polymer segments confined on the silica surface. Both these conformations are detrimental for the hyper-crosslinking reaction. In the first case (MSN_5PVBC, with lower grafting density, high polymer/solvent interactions and fully extended conformation) the polymer/polymer interactions necessary for the extensive hyper-crosslinking are reduced, while in the second case (MSN_20PVBC, with higher grafting density, shorter polymer segments confined to silica surface and high silica/polymer interactions) the polymer segment mobility necessary for the extensive hyper-crosslinking is strongly inhibited. In our set of experiments, the optimal conditions are reached for the sample MSN_10PVBC, in which the intermediate polymer chain conformation in the swelling solvent possibly favours an extensive hyper-crosslinking, as confirmed by the most pronounced disappearance of the chloromethyl groups in the corresponding X_MSN_10PVBC sample, evidenced by FTIR and NMR (Figure 4a-b), and the highest BET SSA and pore volume registered by nitrogen adsorption analysis (Table 1).

3.4 Adsorption Tests

To validate the adsorption capacity of the X_MSN_10PVBC nanoparticles, tailored in terms of amount of hyper-crosslinking extent and textural properties, adsorption tests of rhodamine 6G from solution were performed, using plain MSN for comparison. Results show the very good adsorption capacity of X_MSN_10PVBC, with an uptake of about 125 mg/g for highly concentrated rhodamine 6G solution (C_0=1000 mg/L) and a quite complete removal (about 98 %) of the dye in more diluted conditions (C_0=30 mg/L) (Figure 5a-b). The equilibrium adsorption results for X_MSN_10PVBC well fit the Freundlich adsorption isotherm, which reflects the multilayer adsorption of Rh6G molecules onto the hyper-crosslinked nanoparticles (Figure 5a and Table S1). MSN, on the other hand, show very low adsorption capacity towards Rh6G.

X_MSN_10PVBC, tested for repeated adsorption cycles, show very high regenerability. Indeed, repeated adsorption cycles of Rh6G at initial concentration of 30 mg/L show an uptake of dye between 98 % and 99 % in three subsequent adsorption tests (see inset in Figure 5b), demonstrating that the nanoparticles are able to desorb completely the adsorbed dye and therefore to guarantee comparable adsorption efficiency in the following adsorption cycles.

The adsorption tests show that X_MSN_10PVBC are very efficient for Rh6G removal also when compared to higher surface area VBC-based hyper-crosslinked resins [14]. Indeed, in comparison to VBC-based hyper-crosslinked resins characterized by SSA of about 1900 m^2/g and pore volume of 1.33 cm^3/g, if considered the normalized adsorption capacity per pore volume, the hyper-crosslinked nanoparticles X_MSN_10PVBC show comparable or even higher performances for Rh6G removal from solutions of concentration up to 500 mg/L [14]. Considered that the MSN contribution to Rh6G adsorption is very low, and that the nature of the hyper-crosslinked resin grafted on MSN is very similar to the one of the 1900 m^2/g SSA hyper-crosslinked resin, the significant adsorption capacity of X_MSN_10PVBC is to be ascribed to the peculiar hierarchical porosity of the nanoparticles. Also, considered that plain MSN show a total pore volume (0.49 cm^3/g) higher than X_MSN_10PVBC (0.45 cm^3/g), it is clear that the creation of a hierarchically porous structure in the synthesized hybrid nanoparticles is of key importance for their adsorption capacity, as shown by the comparison of the values of dye adsorbed per pore volume of X_MSN_10PVBC and MSN (Figure 5d).

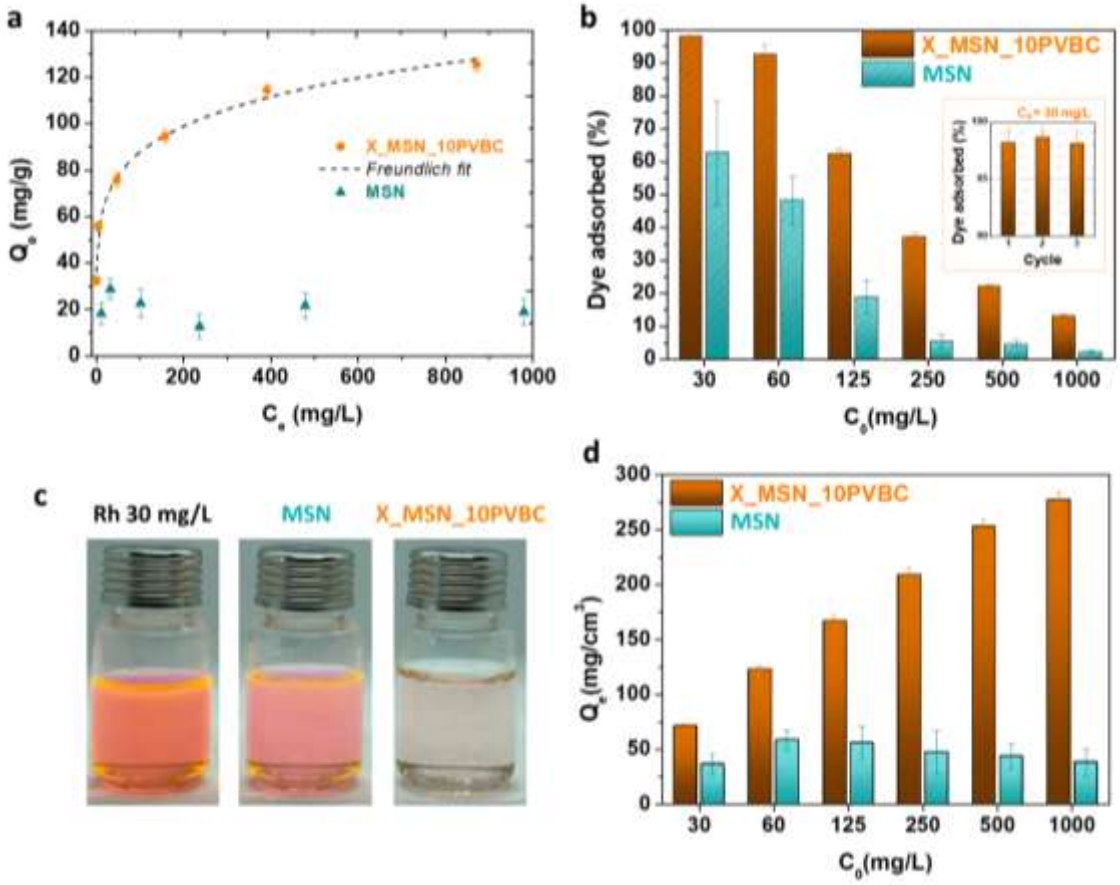

Figure 5. Rhodamine 6G equilibrium adsorption isotherms of X_MSN_10PVBC and MSN (a); adsorbed dye percentage by X_MSN_10PVBC and MSN, with repeated cycles of adsorption of Rh6G at C_0=30 mg/L by

X_MSN_10PVBC in inset (b); images of Rh6G 30 mg/L solution before and after equilibrium adsorption by MSN and X_MSN_10PVBC (c); Rh6G equilibrium adsorption capacity per pore volume of X_MSN_10PVBC and MSN (d).

4. Conclusions

Hierarchically porous silica nanoparticles grafted with hyper-crosslinked poly(vinylbenzyl chloride) are designed and realized in this work. Vinyl functionalized MSN are grafted with PVBC and then the anchored polymer phase is hyper-crosslinked. In this way, the microporosity typical of the hyper-crosslinked resins is generated into the mesopores and wider pores up to 100 nm are created onto the peripheral surface of the MSN. Through optimization of the synthetic procedure, hierarchically porous nanoparticles characterized by about 50 % of organic phase grafted, and constituted by a MSN-templated hierarchical porous structure with up to 28 % of microporosity, are obtained. These nanoparticles result very efficient in the adsorption of organic pollutants from aqueous solution, as demonstrated by rhodamine 6G adsorption tests, showing significantly higher uptake with respect to plain mesoporous silica nanoparticles characterized by higher SSA and pore volume. The hyper-crosslinked PVBC-grafted MSN show a dye uptake of about 125 mg/g in highly concentrated solution (1000 mg/L) and quite complete removal (about 98 %) in more diluted conditions (up to 30 mg/L), with high efficiency in successive adsorption-desorption cycles. Therefore, results demonstrate that the peculiar hierarchically porous structure obtained by grafting of MSN with hyper-crosslinked PVBC is an effective strategy to significantly enhance the MSN performances in an environmental-relevant application such as water remediation.

References

[1] X. Y. Yang, L. H. Chen, Y. Li, J. C. Rooke, C. Sanchez, B. L. Su, Hierarchically porous materials: synthesis strategies and structure design. Chem. Soc. Rev. 46 (2017) 481–558. https://doi.org/10.1039/c6cs00829a.

[2] C.M.A. Parlett, K. Wilson, A.F. Lee, Hierarchical porous materials: Catalytic applications, Chem. Soc. Rev. 42 (2013) 3876–3893. https://doi.org/10.1039/C2CS35378D.

[3] Y. Shi, X. Li, J. Hu, J. Lu, Y. Ma, Y. Zhang, Y. Tang, Zeolite microspheres with hierarchical structures: Formation, mechanism and catalytic performance, J. Mater. Chem. 21 (2011) 16223–16230. https://doi.org/10.1039/c1jm11669j.

[4] X.Y. Yang, L.H. Chen, Y. Li, J.C. Rooke, C. Sanchez, B.L. Su, Hierarchically porous materials: Synthesis strategies and structure design, Chem. Soc. Rev. 46 (2017) 481–558. https://doi.org/10.1039/c6cs00829a.

[5] R.W. Fu, Z.H. Li, Y.R. Liang, F. Li, F. Xu, D.C. Wu, Hierarchical porous carbons: design, preparation, and performance in energy storage, Xinxing Tan Cailiao/New Carbon Mater. 26 (2011) 171–179. https://doi.org/10.1016/S1872-5805(11)60074-7.

[6] F. Scalera, A. Quarta, D.M. Tobaldi, R.C. Pullar, C. Piccirillo, Cork-derived hierarchically porous hydroxyapatite with different stoichiometries for biomedical and environmental applications, Mater. Chem. Front. 5 (2021) 5071–5081. https://doi.org/10.1039/d1qm00584g.

[7] N. Li, D. Niu, Y. Jiang, C. Xu, S. Pan, J. He, J. Chen, L. Zhang, Y. Li, Morphology Evolution and Spatially Selective Functionalization of Hierarchically Porous Silica Nanospheres for Improved Multidrug Delivery, Chem. Mater. 29 (2017) 10377–10385. https://doi.org/10.1021/acs.chemmater.7b03735.

[8] P. Hainey, I.M. Huxham, B. Rowatt, D.C. Sherrington, L. Tetley, Synthesis and Ultrastructural Studies, of Styrene-Divinylbenzene Polyhipe Polymers, Macromolecules. 24 (1991) 117–121. https://doi.org/10.1021/ma00001a019.

[9] R. Castaldo, R. Avolio, M. Cocca, M.E. Errico, M. Avella, G. Gentile, Amino-functionalized hyper-crosslinked resins for enhanced adsorption of carbon dioxide and polar dyes, Chem. Eng. J. 418 (2021) 129463. https://doi.org/10.1016/j.cej.2021.129463.

449 [10] Y. Yu, M. Yang, Z. Yan, T. Li, Q. Jing, P. Liu, B. Xu, J. Cao, Regulation of hierarchically porous structures
450 based on multi-scale nanosheets derived from kaolinite for enhanced adsorption, Appl. Clay Sci. 200
451 (2021) 105895. https://doi.org/10.1016/j.clay.2020.105895.
452 [11] C. Duan, L. Dong, F. Li, Y. Xie, B. Huang, K. Wang, Y. Yu, H. Xi, Room-Temperature Rapid Synthesis of Two-
453 Dimensional Metal-Organic Framework Nanosheets with Tunable Hierarchical Porosity for Enhanced
454 Adsorption Desulfurization Performance, Ind. Eng. Chem. Res. 59 (2020) 18857–18864.
455 https://doi.org/10.1021/acs.iecr.0c02437.
456 [12] M. Hartmann, W. Schwieger, M. Hartmann, Chem Soc Rev Hierarchically-structured porous materials :,
457 Chem. Soc. Rev. 45 (2016) 3311–3312. https://doi.org/10.1039/vided.
458 [13] Y. Ren, Z. Ma, R.E. Morris, Z. Liu, F. Jiao, S. Dai, P.G. Bruce, A solid with a hierarchical tetramodal micro-
459 meso-macro pore size distribution, Nat. Commun. 4 (2013) 1–7. https://doi.org/10.1038/ncomms3015.
460 [14] R. Castaldo, R. Avolio, M. Cocca, M.E. Errico, M. Lavorgna, J. Šalplachta, C. Santillo, G. Gentile,
461 Hierarchically porous hydrogels and aerogels based on reduced graphene oxide, montmorillonite and
462 hyper-crosslinked resins for water and air remediation, Chem. Eng. J. (2021) 133162.
463 https://doi.org/10.1016/j.cej.2021.133162.
464 [15] R. Castaldo, V. Ambrogi, R. Avolio, M. Cocca, G. Gentile, M. Emanuela Errico, M. Avella, Functional hyper-
465 crosslinked resins with tailored adsorption properties for environmental applications, Chem. Eng. J. 362
466 (2019) 497–503. https://doi.org/10.1016/j.cej.2019.01.054.
467 [16] F. Rizzi, R. Castaldo, T. Latronico, P. Lasala, G. Gentile, M. Lavorgna, M. Striccoli, A. Agostiano, R.
468 Comparelli, N. Depalo, M.L. Curri, E. Fanizza, High Surface Area Mesoporous Silica Nanoparticles with
469 Tunable Size in the Sub-Micrometer Regime : Insights on the Size and Porosity Control Mechanisms,
470 (2021) 1–19.
471 [17] S. Kachbouri, N. Mnasri, E. Elaloui, Y. Moussaoui, Tuning particle morphology of mesoporous silica
472 nanoparticles for adsorption of dyes from aqueous solution, J. Saudi Chem. Soc. 22 (2018) 405–415.
473 https://doi.org/10.1016/j.jscs.2017.08.005.
474 [18] S.H. Wu, H.P. Lin, Synthesis of mesoporous silica nanoparticles, Chem. Soc. Rev. 42 (2013) 3862–3875.
475 https://doi.org/10.1039/c3cs35405a.

[19] I.I. Slowing, J.L. Vivero-Escoto, C.W. Wu, V.S.Y. Lin, Mesoporous silica nanoparticles as controlled release drug delivery and gene transfection carriers, Adv. Drug Deliv. Rev. 60 (2008) 1278–1288. https://doi.org/10.1016/j.addr.2008.03.012.

[20] Y. Wang, Q. Zhao, N. Han, L. Bai, J. Li, J. Liu, E. Che, L. Hu, Q. Zhang, T. Jiang, S. Wang, Mesoporous silica nanoparticles in drug delivery and biomedical applications, Nanomedicine Nanotechnology, Biol. Med. 11 (2015) 313–327. https://doi.org/10.1016/j.nano.2014.09.014.

[21] F. Olivieri, R. Castaldo, M. Cocca, G. Gentile, M. Lavorgna, Mesoporous silica nanoparticles as carriers of active agents for smart anticorrosive organic coatings: A critical review, Nanoscale. 13 (2021) 9091–9111. https://doi.org/10.1039/d1nr01899j.

[22] F. Olivieri, R. Castaldo, M. Cocca, G. Gentile, M. Lavorgna, Innovative Silver-Based Capping System for Mesoporous Silica Nanocarriers Able to Exploit a Twofold Anticorrosive Mechanism in Composite Polymer Coatings: Tailoring Benzotriazole Release and Capturing Chloride Ions, ACS Appl. Mater. Interfaces. 13 (2021) 48141–48152. https://doi.org/10.1021/acsami.1c15231.

[23] R. Castaldo, M.S. de Luna, C. Siviello, G. Gentile, M. Lavorgna, E. Amendola, M. Cocca, On the acid-responsive release of benzotriazole from engineered mesoporous silica nanoparticles for corrosion protection of metal surfaces, J. Cult. Herit. 44 (2020) 317–324. https://doi.org/10.1016/j.culher.2020.01.016.

[24] J. Chen, Y. Sheng, Y. Song, M. Chang, X. Zhang, L. Cui, D. Meng, H. Zhu, Z. Shi, H. Zou, Multimorphology Mesoporous Silica Nanoparticles for Dye Adsorption and Multicolor Luminescence Applications, ACS Sustain. Chem. Eng. 6 (2018) 3533–3545. https://doi.org/10.1021/acssuschemeng.7b03849.

[25] A. Feinle, M.S. Elsaesser, N. Hüsing, Sol-gel synthesis of monolithic materials with hierarchical porosity, Chem. Soc. Rev. 45 (2016) 3377–3399. https://doi.org/10.1039/c5cs00710k.

[26] A.H. Karim, A.A. Jalil, S. Triwahyono, S.M. Sidik, N.H.N. Kamarudin, R. Jusoh, N.W.C. Jusoh, B.H. Hameed, Amino modified mesostructured silica nanoparticles for efficient adsorption of methylene blue, J. Colloid Interface Sci. 386 (2012) 307–314. https://doi.org/10.1016/j.jcis.2012.07.043.

[27] H. Nishihara, S.R. Mukai, D. Yamashita, H. Tamon, Ordered macroporous silica by ice templating, Chem. Mater. 17 (2005) 683–689. https://doi.org/10.1021/cm048725f.

503 [28] M. Guerritore, R. Castaldo, B. Silvestri, R. Avolio, M. Cocca, M.E. Errico, M. Avella, G. Gentile, V. Ambrogi,
504 Hyper-crosslinked polymer nanocomposites containing mesoporous silica nanoparticles with enhanced
505 adsorption towards polar dyes, Polymers (Basel). 12 (2020). https://doi.org/10.3390/polym12061388.
506 [29] R. Castaldo, R. Avolio, M. Cocca, G. Gentile, M.E. Errico, M. Avella, C. Carfagna, V. Ambrogi, A Versatile
507 Synthetic Approach toward Hyper-Cross-Linked Styrene-Based Polymers and Nanocomposites,
508 Macromolecules. 50 (2017) 4132–4143. https://doi.org/10.1021/acs.macromol.7b00812.
509 [30] Y.P. Chang, C.L. Ren, Q. Yang, Z.Y. Zhang, L.J. Dong, X.G. Chen, D.S. Xue, Preparation and characterization
510 of hexadecyl functionalized magnetic silica nanoparticles and its application in Rhodamine 6G removal,
511 Appl. Surf. Sci. 257 (2011) 8610–8616. https://doi.org/10.1016/j.apsusc.2011.05.031.
512 [31] E. Pino, C. Calderón, F. Herrera, G. Cifuentes, G. Arteaga, Photocatalytic Degradation of Aqueous
513 Rhodamine 6G Using Supported TiO2 Catalysts. A Model for the Removal of Organic Contaminants From
514 Aqueous Samples, Front. Chem. 8 (2020) 1–12. https://doi.org/10.3389/fchem.2020.00365.
515 [32] F. Gomri, G. Finqueneisel, T. Zimny, S.A. Korili, A. Gil, M. Boutahala, Adsorption of Rhodamine 6G and
516 humic acids on composite bentonite–alginate in single and binary systems, Appl. Water Sci. 8 (2018) 1–
517 10. https://doi.org/10.1007/s13201-018-0823-6.
518 [33] G. Annadurai, R.S. Juang, D.J. Lee, Adsorption of rhodamine 6G from aqueous solutions on activated
519 carbon, J. Environ. Sci. Heal. - Part A Toxic/Hazardous Subst. Environ. Eng. 36 (2001) 715–725.
520 https://doi.org/10.1081/ESE-100103755.
521 [34] P. Qin, Y. Yang, X. Zhang, J. Niu, H. Yang, S. Tian, J. Zhu, M. Lu, Highly efficient, rapid, and simultaneous
522 removal of cationic dyes from aqueous solution using monodispersed mesoporous silica nanoparticles
523 as the adsorbent, Nanomaterials. 8 (2018). https://doi.org/10.3390/nano8010004.
524 [35] N. Abidi, E. Hequet, S. Tarimala, Functionalization of Cotton Fabric with Vinyltrimethoxysilane, Text. Res.
525 J. 77 (2007) 668–674. https://doi.org/10.1177/0040517507080621.
526 [36] N. hsuan Hu, J.C. Furgal, R-silsesquioxane-based network polymers by fluoride catalyzed synthesis: An
527 investigation of cross-linker structure and its influence on porosity, Materials (Basel). 13 (2020) 24–29.
528 https://doi.org/10.3390/MA13081849.

[37] R. Avolio, G. Gentile, M. Avella, D. Capitani, M.E. Errico, Synthesis and characterization of poly(methylmethacrylate)/silica nanocomposites: Study of the interphase by solid-state NMR and structure/properties relationships, J. Polym. Sci. Part A Polym. Chem. 48 (2010) 5618–5629. https://doi.org/10.1002/pola.24377.

[38] C. Wang, H. Yang, F. Chen, L. Peng, H. fang Gao, L. ping Zhao, Influences of VTMS/SiO2 ratios on the contact angle and morphology of modified super-hydrophobic silicon dioxide material by vinyl trimethoxy silane, Results Phys. 10 (2018) 891–902. https://doi.org/10.1016/j.rinp.2018.08.007.

[39] J. Li, P. Wei, L. Li, Y. Qian, C. Wang, N.H. Huang, Synergistic effect of mesoporous silica SBA-15 on intumescent flame-retardant polypropylene, Fire Mater. 35 (2011) 83–91. https://doi.org/10.1002/FAM.1040.

[40] P. Wang, J. Dai, Y. Ma, L. Chen, J. Pan, Fabrication and evaluation of aminoethyl benzo-12-crown-4 functionalized polymer brushes adsorbents formed by surface-initiated ATRP based on macroporous polyHIPEs and postsynthetic modification, Chem. Eng. J. 380 (2020) 122495. https://doi.org/10.1016/j.cej.2019.122495.

[41] J.D. Webb, T. Seki, J.F. Goldston, M. Pruski, C.M. Crudden, Selective functionalization of the mesopores of SBA-15, Microporous Mesoporous Mater. 203 (2015) 123–131. https://doi.org/10.1016/j.micromeso.2014.10.032.

[42] R. Castaldo, G. Gentile, M. Avella, C. Carfagna, V. Ambrogi, Microporous hyper-crosslinked polystyrenes and nanocomposites with high adsorption properties: A review, Polymers (Basel). 9 (2017). https://doi.org/10.3390/polym9120651.

[43] R. Castaldo, R. Avolio, M. Cocca, G. Gentile, M.E. Errico, M. Avella, C. Carfagna, V. Ambrogi, Synthesis and adsorption study of hyper-crosslinked styrene-based nanocomposites containing multi-walled carbon nanotubes, RSC Adv. 7 (2017) 6865–6874. https://doi.org/10.1039/c6ra25481k.

[44] M.A. Isaacs, N. Robinson, B. Barbero, L.J. Durndell, J.C. Manayil, C.M.A. Parlett, C. D'Agostino, K. Wilson, A.F. Lee, Unravelling mass transport in hierarchically porous catalysts, J. Mater. Chem. A. 7 (2019) 11814–11825. https://doi.org/10.1039/c9ta01867k.

555 [45] J. Midya, Y. Cang, S.A. Egorov, K. Matyjaszewski, M.R. Bockstaller, A. Nikoubashman, G. Fytas,
556 Disentangling the Role of Chain Conformation on the Mechanics of Polymer Tethered Particle Materials,
557 Nano Lett. 19 (2019) 2715–2722. https://doi.org/10.1021/acs.nanolett.9b00817.
558 [46] Y.G. Kim, H. Thérien-Aubin, Impact of the Solvent Quality on the Local Dynamics of Soft and Swollen
559 Polymer Nanoparticles Functionalized with Polymer Chains, Macromolecules. 53 (2020) 7561–7569.
560 https://doi.org/10.1021/acs.macromol.0c00346.